Journal of
**Synchrotron
Radiation**

ISSN 0909-0495

Received 23 June 2009
Accepted 31 August 2009

Linear polarization scans for resonant X-ray diffraction with a double-phase-plate configuration

Valerio Scagnoli,* Claudio Mazzoli, Carsten Detlefs, Pascal Bernard, Andrea Fondacaro, Luigi Paolasini, Federica Fabrizi and Francois de Bergevin

European Synchrotron Radiation Facility, BP 220, 38043 Grenoble Cedex 9, France.
E-mail: scagnoli@esrf.eu

An in-vacuum double-phase-plate diffractometer for performing polarization scans combined with resonant X-ray diffraction experiments is presented. The use of two phase plates enables the correction of some of the aberration effects owing to the divergence of the beam and its energy spread. A higher rate of rotated polarization is thus obtained in comparison with a system with only a single retarder. Consequently, thinner phase plates can be used to obtain the required rotated polarization rate. These results are particularly interesting for applications at low energy (*e.g.* 4 keV) where the absorption owing to the phase plate(s) plays a key role in the feasibility of these experiments. Measurements by means of polarization scans at the uranium M_4 edge on UO_2 enable the contributions of the magnetic and quadrupole ordering in the material to be disentangled.

Keywords: X-ray diffraction; magnetic scattering; phase plate; polarization.

1. Introduction

Resonant X-ray diffraction has become in the last decade a powerful tool for the study of charge, magnetic and orbital degrees of freedom in a wide variety of physical systems (Gibbs *et al.*, 1988; Murakami *et al.*, 1998). By tuning the energy of the incident photons to a given absorption edge it provides site-specific information and also, in general, an enhancement of the observed signal of several orders of magnitude. The most striking examples are the resonances at the uranium M_4 and M_5 edges (Isaacs *et al.*, 1989). As a result, even usually weak signals such as those from X-ray magnetic scattering can be measured and give precious and complementary information to that obtained by neutron scattering (Scagnoli *et al.*, 2006; Fabrizi *et al.*, 2009).

It is not always straightforward to establish the source of the resonant diffracted intensities, however. Several contributions might be present at the same time, such as the anisotropy of the tensor of susceptibility (Templeton & Templeton, 1982). In addition, different resonant events, *e.g.* dipole–dipole ($E1$–$E1$), quadrupole–quadrupole ($E2$–$E2$) and dipole–quadrupole ($E1$–$E2$), might be present (Paolasini *et al.*, 1999). In order to extract valuable information and to disentangle different contributions that might be present at the same time, polarization analysis of the scattered beam and scans of the scattering wavevector, the so-called azimuthal scan, can be used. Hill & McMorrow (1996) have given a full account of the polarization dependence of the X-ray magnetic scattering length.

While azimuthal scans often provide unique information for disentangling different contributions, they are severely limited by the set-up geometry and sample environment. In a conventional set-up the diffraction geometry is limited to only two of the four polarization channels. Rotating the polarization of the incident X-rays offers the appealing possibility to access the other two polarization channels.

Recently, a new method of extracting information by means of resonant X-ray scattering has been presented (Mazzoli *et al.*, 2007). It consists of studying the polarization dependence of the diffracted intensities as a function of the direction of the (linear) polarization of the X-rays impinging on the sample. Such a scan is referred to as an incident polarization scan or, in short, a ‘polscan’. A subtle interference between purely dipole ($E1$–$E1$) and purely quadrupole ($E2$–$E2$) transitions, leading to a phase shift between the respective scattering amplitudes, was observed. This effect may be exploited to disentangle two close-lying resonances that appear as a single peak in a conventional energy scan, in this way allowing the different multipole order parameters involved to be singled out and identified. The same method was used in $TbMn_2O_5$ to refine the spin orientation of the terbium ion substructure (Johnson *et al.*, 2008).

Resonant X-ray diffraction is mostly employed to study $3d$ transition ions and $4f$ systems. Thus the energy range generally used is between 3 and 10 keV. In this energy range the most effective way to rotate the X-ray polarization is to use as a phase plate a perfect crystal close to a Bragg reflection (Golovchenko *et al.*, 1986; Hirano *et al.*, 1991). Dynamical diffraction theory predicts that the plate shifts the relative phases of two orthogonal polarization components. The phase shift $\Delta\varphi$ depends on the thickness of the plate and on the offset from the Bragg position. The main drawbacks are the imperfect collimation and chromaticity which lead to some depolarization. This can be reduced by using a thicker plate which in turn may strongly absorb the beam. Even using diamond, the lightest perfect crystal, at very low energies the plate thickness represents a major constraint to the feasibility of experiments. Absorption might dramatically reduce the signal below the detection threshold. In an effort to minimize the plate absorption, two diamonds, instead of a single one, can be used. The two retarders compensate one another in some of the depolarizing effects. With the same equivalent thickness a better rate of rotated polarization is thus obtained (Okitsu *et al.*, 2001). Therefore, the same rotated polarization rate can be achieved using two thinner diamonds.

To summarize, for resonant X-ray diffraction experiments with incident polarization scans it is important to achieve the best performance out of the phase plates by minimizing their absorption and enhancing the rotated polarization rate. These two requirements are both met by the combined use of two phase plates.

The layout of the paper is as follows. §2 introduces the Stokes parameters and describes how to perform a polarization scan by means of diamond phase plates. §3 illustrates the advantages of using a double phase plate compared with a set-up with a single phase plate. In §4 we describe the in-vacuum diffractometer designed to align the two phase plates and to perform polarization scans. §5 gathers the results obtained at different energies and quantifies the different performances of a single- and a double-phase-plate set-up. §6 describes a practical application: polarization scans, performed with a pair of 0.05 mm-thick diamonds, are employed at the uranium M_4 edge in UO_2 to disentangle the magnetic and quadrupolar ordering which take place below the antiferromagnetic ordering temperature. Finally, §7 contains our conclusions.

2. Stokes parameters and polarization scans

The polarization state of an X-ray beam is most easily described in the Poincaré–Stokes notation (Blume & Gibbs, 1988; Born & Wolf, 1999). The Stokes parameters P_1, P_2 and P_3 describe the rate of linear polarization in the horizontal plane, in a plane rotated by 45° around the beam with respect to the horizontal, and circular polarization, respectively. For a plane wave with electric field amplitudes E_h and E_v in the horizontal and vertical planes, respectively, the Stokes parameters are given by (Fano, 1957; Blume & Gibbs, 1988)

$$P_1 = \frac{|E_h|^2 - |E_v|^2}{|E_h|^2 + |E_v|^2}, \tag{1}$$

$$P_2 = \frac{|E_h + E_v|^2 - |E_h - E_v|^2}{2\left(|E_h|^2 + |E_v|^2\right)}, \tag{2}$$

$$P_3 = \frac{|E_h + iE_v|^2 - |E_h - iE_v|^2}{2\left(|E_h|^2 + |E_v|^2\right)}. \tag{3}$$

We define the density matrix

$$\rho = (1/2)\, I\,(1 + \boldsymbol{\sigma}\cdot\mathbf{P}),$$

where $I = |E_h|^2 + |E_v|^2$ is the intensity of the beam, $\mathbf{P} = (P_1, P_2, P_3)$ is the Stokes polarization vector, and $\boldsymbol{\sigma}$ represents the Pauli matrices

$$\boldsymbol{\sigma}_1 = \begin{pmatrix} 1 & 0 \\ 0 & -1 \end{pmatrix},\ \boldsymbol{\sigma}_2 = \begin{pmatrix} 0 & 1 \\ 1 & 0 \end{pmatrix},\ \boldsymbol{\sigma}_3 = \begin{pmatrix} 0 & -i \\ i & 0 \end{pmatrix}. \tag{4}$$

Note that this is not the standard convention for the Pauli matrices.

The natural horizontal polarization of synchrotron radiation from a planar undulator source is described by

$$\boldsymbol{\rho} = I \begin{pmatrix} 1 & 0 \\ 0 & 0 \end{pmatrix}, \tag{5}$$

i.e. (perfect) linear polarization in the horizontal plane. Let $\mathbf{M}$ describe the diffraction process of an X-ray optical element, such as a phase plate, a sample or a polarization analyzer. The density matrix of the scattered beam is then given by

$$\boldsymbol{\rho}' = \mathbf{M}\cdot\boldsymbol{\rho}\cdot\mathbf{M}^{\dagger}, \tag{6}$$

$$I' = \mathrm{tr}(\boldsymbol{\rho}'), \tag{7}$$

$$\mathbf{P}' = \frac{\mathrm{tr}(\boldsymbol{\sigma}\cdot\boldsymbol{\rho}')}{\mathrm{tr}(\boldsymbol{\rho}')}. \tag{8}$$

The transfer matrices for Thomson, non-resonant and resonant magnetic scattering have been discussed in detail (Blume & Gibbs, 1988; Hill & McMorrow, 1996).

We recall that the relative phase shift, $\Delta\varphi$, in the transmitted beam between the X-rays with polarization perpendicular (σ) and parallel (π) to the scattering plane of the phase plate is given by Giles *et al.* (1994),

$$\Delta\varphi = -\frac{\pi}{2}\left(\frac{r_e^2}{\pi^2}\frac{F_h F_{\bar{h}}}{V^2}\frac{\lambda^3 \sin 2\theta_B}{\Delta\theta}\right)t, \tag{9}$$

where F_h and θ_B are the structure factor and the Bragg angle of the excited reflection, r_e is the classical electron radius, V is the unit cell volume, λ is the X-ray wavelength, and t is the thickness of the crystal. $\Delta\theta$ represents the misalignment relative to the Bragg condition. It is therefore desirable to use thin crystals (to minimize absorption), and not to work too close to the Bragg condition, *i.e.* at $\Delta\theta$ much larger than the divergence of the beam and the mosaicity of the crystal. At a given wavelength, one thus has to select a crystal with a large structure factor per unit volume, F_h/V, small mosaicity, and low X-ray absorption. High-quality diamond crystals perfectly fulfil these requirements. In particular, the [111] reflection gives the best results as it has the largest value for the structure factor.

For an X-ray phase plate with vertical scattering plane, the matrix is given by

$$\mathbf{M}_0 \propto \begin{pmatrix} 1 & 0 \\ 0 & \exp(i\Delta\varphi) \end{pmatrix}, \tag{10}$$

where $\Delta\varphi$ is given by (9). Upon rotating the scattering plane through χ around the beam, the matrix transforms as

$$\begin{aligned}\mathbf{M} &= \mathbf{R} \cdot \mathbf{M}_0 \cdot \mathbf{R}^{-1} \\ &= 1 + \frac{[\exp(i\Delta\varphi) - 1]}{2}\Big(1 - \boldsymbol{\sigma}_2 \sin 2\chi - \boldsymbol{\sigma}_1 \cos 2\chi\Big),\end{aligned} \tag{11}$$

where

$$\mathbf{R} = \begin{pmatrix} \cos\chi & -\sin\chi \\ \sin\chi & \cos\chi \end{pmatrix}. \tag{12}$$

The resulting polarization parameters are

$$P_1' = 1 + [\cos(\Delta\varphi) - 1]\sin(2\chi)^2, \tag{13}$$

$$P_2' = \sin(\Delta\varphi/2)^2 \sin(4\chi), \tag{14}$$

$$P_3' = -\sin(\Delta\varphi)\sin(2\chi). \tag{15}$$

We note that for all $\Delta\varphi$ and χ the beam is perfectly polarized $[(P_1')^2 + (P_2')^2 + (P_3')^2 = 1]$. Furthermore, for $\Delta\varphi = 0, \pm\pi, \pm 2\pi, \ldots$, the beam is linearly polarized ($P_3 = 0$). In this setting the phase plate may be used to rotate the plane of polarization around the beam. The direction of the photon polarization is rotated by an arbitrary angle $\zeta = 2\chi$ (Fig. 1). For the production of circularly polarized X-rays ($\Delta\varphi = \pm\pi/2$), following (15) the scattering plane has to be rotated around the beam to form an angle $\chi = 45°$ with the plane of the synchrotron and $\Delta\theta_{\rm circ} \simeq 2\Delta\theta$, where $\Delta\theta$ represents the misalignment relative to the Bragg condition for rotated linear light.

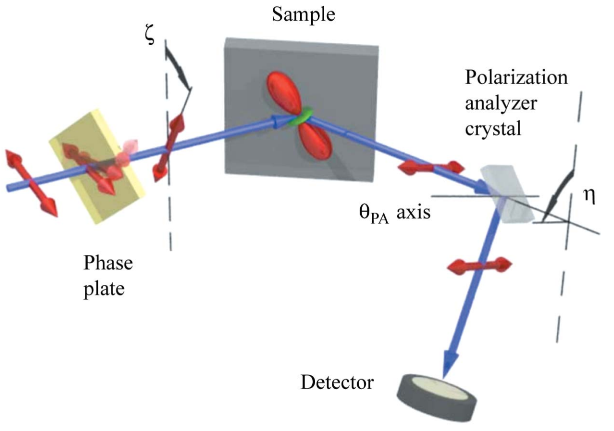

Figure 1
Experimental set-up with a phase plate. X-ray propagation directions are indicated by blue arrows, polarizations by red ones. Synchrotron light arrives from the left, horizontally polarized (π). $\zeta = 2\chi$ is the rotation angle of the incident polarization. η is the rotation angle of the polarization analyzer crystal; the zero positions of the two angles, corresponding to σ and σ' polarizations, respectively, are represented by dashed lines. The solid line is the rocking axis of the polarization analysis crystal $\theta_{\rm PA}$. (Reproduced from Mazzoli *et al.*, 2007.)

3. Double phase plates compared with a single one

In this section we show that a double-phase-plate device can be operated in four modes, one of them equivalent to a single plate and each of the other three compensating for two of three defects, which are the divergences in two perpendicular directions and the achromaticity (energy dispersion).

The double-phase-plate diffractometer can be operated in different modes: let the angle between the beam and the lattice planes of a plate be

$$\theta = \pm(\theta_{\rm B} + \Delta\theta). \tag{16}$$

The sign of the angular offset $\Delta\theta$ from the Bragg angle $\theta_{\rm B}$ is the sign of the phase lag of the π polarization relative to the σ polarization. We observe that rotating χ, *i.e.* the azimuth of the plate about the beam, by 180° is equivalent to a sign change in θ [but not in $\Delta\theta$ defined in (16)]; and rotating χ by 90° exchanges the σ and π polarization directions. Consider two phase plates, subscripted 1 and 2, of equal thickness, tuned at offsets $|\Delta\theta_1| = |\Delta\theta_2| = \Delta\theta$. They produce the same phase lag, and the signs of $\Delta\theta_1$ and $\Delta\theta_2$ should be such that those lags add. In the first configuration $\chi_1 = \chi_2$, $\theta_1 = \theta_2$, then in the three others χ_2 is rotated by 90° in sequence while leaving χ_1, θ_1, θ_2 unchanged. Call these configurations (I), (II), (III) and (IV) (Fig. 2). Configuration (I) is equivalent to one single phase plate whose thickness is the sum of both.

In configuration (III) ($\chi_1 = \chi_2 + 180°$), the σ and π directions are again common to both plates, and, with $\Delta\theta$ being the same, the phase lags add as in (I), but, when referred to a common axis, θ_1 and θ_2 are now opposite. A ray inclined by $\delta\theta$ in the common diffraction plane sees the lattice planes at the angles

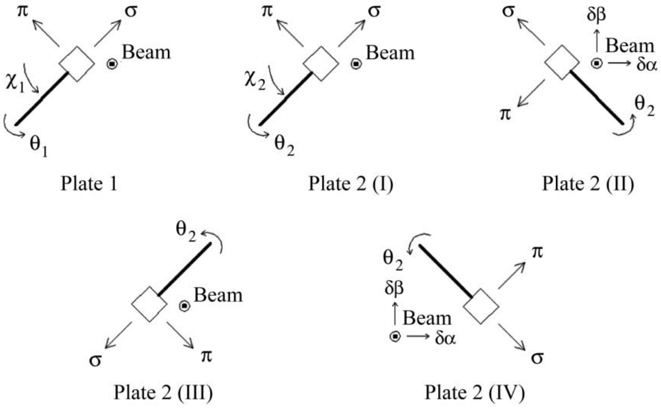

Figure 2
Configurations of the two phase plates, 1 and 2, as viewed when looking along the beam. The configuration of plate 1 is drawn, then four possible configurations of plate 2. Plate 1 is fixed. The difference in azimuths about the beam, $\chi_2 - \chi_1$, is set at 0°, 90°, 180° and 270° for configurations (I), (II), (III) and (IV), respectively. The angle θ_2 of plate 2 lattice planes with the beam is set to θ_1 in configurations (I) and (III) but is different in (II) and (IV) (see text). In these latter cases the σ and π directions are exchanged from one plate to the other, the diffraction plane being defined by the beam and the π direction. In these two cases the rays deviating by angles $\delta\alpha$ and $\delta\beta$ from the mean ray, in the planes bisecting the diffraction planes of the two plates, behave differently (see text).

$$\theta_1' = \theta_{\rm B} + (\Delta\theta - \delta\theta) \quad \text{and} \quad \theta_2' = -\big[\theta_{\rm B} + (\Delta\theta + \delta\theta)\big]. \quad (17)$$

The offset errors $\pm\delta\theta$ are opposite and so are the phase lag errors, which cancel to first order. A ray inclined in the perpendicular direction has no θ offset to first order. Therefore all angular deviations are ineffective to first order. If a ray with the correct direction has an energy with a Bragg angle $\theta_{\rm B}' = \theta_{\rm B} + \delta\theta$, we may substitute for $\theta_{\rm B}$ in (16),

$$\theta_1 = \theta_{\rm B}' + (\Delta\theta - \delta\theta) \quad \text{and} \quad \theta_2 = -\big[\theta_{\rm B}' + (\Delta\theta - \delta\theta)\big]. \quad (18)$$

This defect produces phase lag errors from both plates, which add. It is not compensated for.

In configurations (II) and (IV), in order to add phase lags, and because the σ and π directions are exchanged between the two plates, the signs of angular offsets should be opposite,

$$\theta_1 = \theta_{\rm B} + \Delta\theta \quad \text{and} \quad \theta_2 = \theta_{\rm B} - \Delta\theta. \quad (19)$$

Now a ray at a different energy undergoes two opposite phase lag errors which compensate to first order. In (II) a ray deviating by $\delta\alpha$ in the horizontal plane in Fig. 2 travels at θ angles

$$\theta_1' = \theta_{\rm B} + (\Delta\theta - \delta\alpha/\sqrt{2}) \quad \text{and} \quad \theta_2' = \theta_{\rm B} - (\Delta\theta + \delta\alpha/\sqrt{2}), \quad (20)$$

so that the errors in offsets are opposite and compensate each other. A ray deviating by $\delta\beta$ in the perpendicular direction travels with angular errors whose relative signs are changed from the above and do not compensate. In (IV) the role of both directions is exchanged: compensation is therefore a deviation as $\delta\beta$ but not for one as $\delta\alpha$. The results are summarized in Table 1, where a (+) sign indicates a compensation and a (−) sign indicates no compensation.

The discussion began with $\theta_2 = \theta_1$ in configuration (I). If instead the initial setting is $\theta_2 = -\theta_1$, the properties of (I) and (III) are simply exchanged, as those of (II) and (IV). A further effect should be accounted for, the correlation between chromaticity and angular deviation in the vertical plane, produced by the monochromator. This correlation is modified, and its sign possibly inverted, by any focusing element inserted between the monochromator and the phase plates. This is not discussed here.

The compensation of defects was demonstrated as effective (Okitsu *et al.*, 2001). A preliminary experiment was also performed on ID20 (Giles *et al.*, 1997), showing at 10.44 keV an improvement of the polarization, in the extreme case, from $P_1' = -0.6$ to $P_1' = -0.8$.

4. Double-phase-plate in-vacuum diffractometer

To maximize the amount of rotated and transmitted light, we have developed an in-vacuum double-phase-plate diffractometer, following the results of Okitsu *et al.* (2001). It is currently installed at the magnetic scattering beamline ID20 (Paolasini *et al.*, 2007) of the European Synchrotron Radiation Facility, Grenoble, France.

Fig. 3 shows a schematic view of the diffractometer. It is composed of six circles (θ_1, θ_2, χ_1, χ_2, α and μ) plus two motorized translations (x and z) in order to align the two retarders with suitable accuracy.

Table 1
Errors compensated for in configurations (I)–(IV).

(+): compensation; (−): no compensation. δE is the energy error, $\delta\alpha$ and $\delta\beta$ are angular deviations (Fig. 2).

Configuration	δE	$\delta\alpha$	$\delta\beta$
(I)	(−)	(−)	(−)
(II)	(+)	(+)	(−)
(III)	(−)	(+)	(+)
(IV)	(+)	(−)	(+)

The fine positioning of the two diamond phase plates (to ensure the correct phase shifts, $\Delta\theta_1$ and $\Delta\theta_2$) is obtained by use of two Newport Microcontrole URS100 rotation stages with resolution 0.2 mdeg (0.72 arcsec). The rotation stages are equipped with Renishaw encoders having a resolution of 0.1 mdeg (0.36 arcsec). The rotation of the direction of the polarization is obtained by two concentric Huber rotation stages (model 410 for the first phase plate and 408 for the second). Therefore, the two phase plates can be rotated about the beam direction independently by sweeping angles χ_1 and χ_2. This degree of freedom plays an important role as different double-phase-plate configurations are possible in order to correct, for each configuration, some but not all of the aberrations present in the X-ray beam (see §3). The α, μ, x and z degrees of freedom are needed in order to have the χ_1, χ_2 axes of rotation exactly parallel to the beam direction. There are two translations (x and z) which form a left-handed orthogonal reference system with the beam direction (y). Finally two rotations, combined with the translations, enable the rotation axis defined by the two Huber rotating stages to be placed parallel to the beam direction.

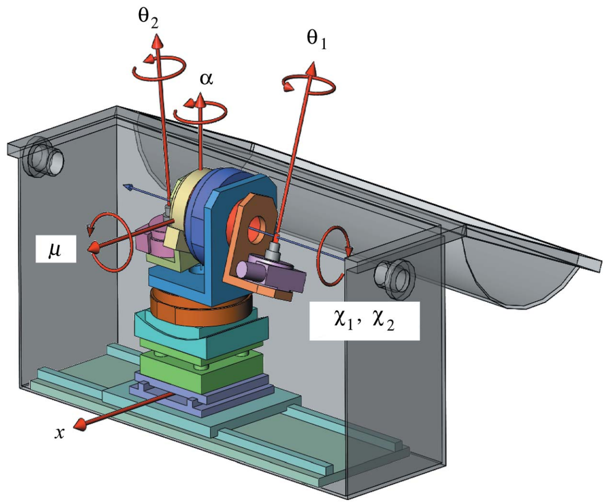

Figure 3
Schematic of the double-phase-plate diffractometer. The two phase plates can be mounted on the rotating stages θ_1 and θ_2. The χ_1 and χ_2 circles provide rotation about the X-ray beam. α and μ enable the χ_1 and χ_2 rotation axes to be parallel to the beam. Finally, x and z (which coincides with the α rotation axis for $\mu = 0$) allows the diffractometer to shift rigidly along the respective directions.

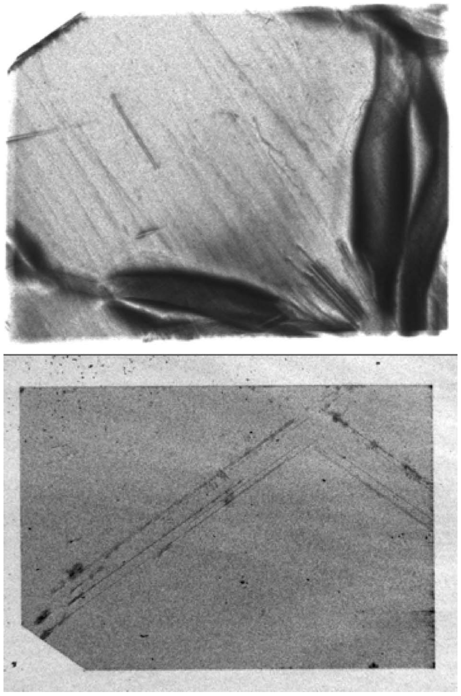

Figure 4
White-beam topography of the (220) reflection for two typical phase plates made from synthetic diamonds produced by the high-pressure high-temperature method. The top panel refers to an older plate made from type-Ib material (nitrogen-rich, 100 p.p.m.); it shows mainly images of dislocations and strain fields related to growth sector boundaries. The lower panel shows a recently produced plate made from type-IIa material (very low nitrogen concentration, less then 0.1 p.p.m.). Only a few dislocation lines, related to stacking faults which are out of contrast, are present.

The diamond phase plates have polished (110) faces. They are aligned in the sample holder in a (110)–$(1\bar{1}1)$ zone, so that the $(1\bar{1}1)$ reflection can easily be used in the symmetric Laue geometry.

Diamonds of different thickness are currently available: 2 × 0.05 mm, 2 × 0.1 mm, 2 × 0.2 mm, 0.3 mm, 0.4 mm, 0.5 mm, 0.72 mm, 1.2 mm. The phase plates (except 0.72 mm and 1.2 mm) were made from locally dislocation-free highly pure (nitrogen content less than 0.1 p.p.m.) type-IIa high-pressure high-temperature material, manufactured by Element Six Technologies, Johannesburg, South Africa.

Fig. 4 shows white-beam topography of the new high-quality diamond compared with an old phase plate.

4.1. Thickness of the phase plate

When selecting the material, thickness and Bragg reflection of the phase plate for a given working energy, one has to compromise between absorption and the quality of polarization. The absorption depends on the photon energy and material only and is thus straightforward to calculate. The quality of polarization depends on more parameters: the use as quarter- or half-wave plate (*i.e.* phase shift $\Delta\varphi = \pi/2$ or π), the divergence and bandwidth of the incident beam, and the crystal quality, see (9). One way of quantifying this problem is to specify the desired working point $\Delta\theta$, and to calculate the corresponding thickness,

$$t = -\frac{2}{\pi}\left[\frac{\pi^2}{r_{\rm e}^2}\frac{V^2}{F_h F_{\bar{h}}}\frac{\Delta\theta\,\Delta\varphi}{\lambda^3\sin(2\theta_{\rm B})}\right], \qquad (21)$$

and compare it with the attenuation length. Modifying the working point $\Delta\theta$ or the required phase shift $\Delta\varphi$ multiplies the entire curve by a corresponding factor, but does not change the energy dependence.

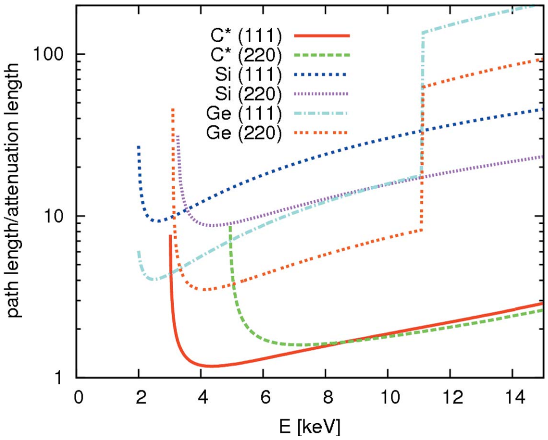

Figure 5
Ratio of the effective path to attenuation length for selected materials as a function of the incident X-ray energy. The effective path is evaluated assuming the phase plate is used under symmetric Laue reflection conditions. C*, Si and Ge stand for diamond, silicon and germanium, respectively.

As an example, we compare diamond, silicon and germanium quarter-wave plates ($\Delta\varphi = \pi/2$), choosing a working point at $\Delta\theta = 0.02^\circ$ (see Fig. 5). Except for the lowest photon energies $E < 3.5$ keV, C* (diamond) offers the best performance. At 4.35 keV, a phase plate of thickness 80 µm gives an X-ray path length in the crystal of ∼120 µm, compared with an attenuation length of ∼100 µm. Note that the optimum thickness for a silicon or germanium phase plate below 3.5 keV is well below 10 µm. Beryllium has a high potential as phase plate material (Giles *et al.*, 1995). To date, however, single crystals of sufficient quality are not widely available. For a given material, *e.g.* diamond, the choice of the Bragg reflection remains. We find that for low energies the (111) reflection gives the best performance, whereas for higher energies the (220) reflection performs slightly better, as the smaller structure factor is compensated by the larger Bragg angle.

5. Results

In the present work we present systematic checks with various energies and plate thicknesses. Three different X-ray incident energies were chosen: 3.720, 5.570 and 7.200 keV, which lie close to the uranium M_4, vanadium K and iron K edge, respectively. In order to measure the rotated polarization rate for each energy the appropriate polarization analyzer crystal was selected [Au(1 1 1), graphite (0 0 4), MgO (2 2 2),

Table 2
Polarization rate (in terms of the Stokes parameters P_1' and P_2') obtained at E = 3.720 keV with double-phase-plate configurations as illustrated in Fig. 2.

Each phase plate has a thickness t = 0.05 mm. Explicit values for the angles χ_1, χ_2, θ_1 and θ_2 are also given. The total effective thickness $t' = t/\cos\theta$ = 0.17 mm. The transmitted beam is 6% of the incident one.

Energy (keV)	χ_1	χ_2	θ_1	θ_2	$P_1' \pm 0.2$	$P_2' \pm 0.2$
3.720 (I)	45	45	+55	+55	−0.87	0.00
3.720 (II)	45	135	+55	−55	−0.95	0.02
3.720 (III)	45	45	+55	−55	−0.91	0.01
3.720 (IV)	45	−45	+55	−55	−0.97	0.03

Table 3
Polarization rate (in terms of the Stokes parameters P_1' and P_2') obtained at E = 5.570 keV with double-phase-plate configurations as illustrated in Fig. 2.

Each phase plate has a thickness t = 0.1 mm. The total effective thickness $t' = t/\cos\theta$ = 0.24 mm, resulting in a transmitted beam which is 32% of the incident one.

Energy (keV)	χ_1	χ_2	θ_1	θ_2	$P_1' \pm 0.2$	$P_2' \pm 0.2$
5.570 (I)	45	45	+33	+33	−0.89	0.01
5.570 (II)	45	135	+33	−33	−0.96	0.03
5.570 (III)	45	45	+33	−33	−0.92	0.01
5.570 (IV)	45	−45	+33	−33	−0.99	0.03

respectively]. Incoming X-ray energies match Bragg's law for the polarization crystal d-spacings in order to have the Bragg angle equal to 45° to fully suppress the polarization component in the polarizer scattering plane.

The polarization state of the X-rays after the phase plate(s) is evaluate by means of

$$I'(\eta) = (I_0/2)(1 + P_1'\cos 2\eta + P_2'\sin 2\eta), \tag{22}$$

where I_0 and I' represent the intensity of the X-rays before and after the phase plate(s), η represents the rotation of the analyzer crystal scattering plane about the incoming beam direction (Fig. 1). P_1' and P_2' are two of the three Stokes parameters introduced previously (primes here indicate that they are evaluated after the retarders). Several rocking curves of the polarizer crystal are collected as a function of η. The integrated intensities are then used to estimate I_0, P_1' and P_2'.

The estimated values of the rotated linear polarization (so-called half-wave mode) for the different photon energies and phase plate configurations are given in Tables 2–5. Configuration (I), equivalent to a single phase plate, gives the poorest rotated polarization rate for all the different incident energies. Configurations (II) and (IV) provide the best results with an improvement in the transmitted polarization rate of roughly 10%. The main error corrected by the presence of the two phase plates is the energy spread of the X-rays coming from the monochromator (see Table 2).

This is illustrated in Fig. 6. Plate 1 is fixed as out-phasing by $\pi/2$ and transforming the linear polarization into circular. The θ angle of plate 2 is scanned. When it passes through positions out-phasing by $\pm\pi/2$ the linear polarization is either rotated by $\pi/2$ (at the minimum of P_1') or restored to its initial direction (at the maximum). The data are intensities measured in the unrotated channel, see (22) with $\eta = 0$, suitably normalized and shifted. Cases (I) and (IV) are shown, together with fitted curves. The fitting function is obtained from P_1', which depends on $\Delta\theta$ through (9) and (13), by the following procedure. Equation (9) is extended to represent the total out-phase from plates 1 and 2, so that P_1' is now a function of $\Delta\theta_1$ and $\Delta\theta_2$ (see details in Appendix B). That function is convoluted with two resolution functions in $(\Delta\theta_1 + \Delta\theta_2)$, $(\Delta\theta_1 - \Delta\theta_2)$. Two angular spreads are then used, just one being compensated. Since this calculation goes beyond the first order considered in §3, some

Table 4
Polarization rate (in terms of the Stokes parameters P_1' and P_2') obtained at E = 7.200 keV with double-phase-plate configurations as illustrated in Fig. 2.

Each phase plate has a thickness t = 0.2 mm. The total effective thickness $t' = t/\cos\theta$ = 0.44 mm. The total transmitted beam is 39% of the incident one.

Energy (keV)	χ_1	χ_2	θ_1	θ_2	$P_1' \pm 0.2$	$P_2' \pm 0.2$
7.200 (I)	45	45	+24.5	+24.5	−0.76	−0.06
7.200 (II)	45	135	+24.5	−24.5	−0.88	−0.05
7.200 (III)	45	45	+24.5	−24.5	−0.78	−0.06
7.200 (IV)	45	−45	+24.5	−24.5	−0.89	−0.05

Table 5
Polarization rate (in terms of the Stokes parameters P_1' and P_2') obtained at E = 7.200 keV with double-phase-plate configurations as illustrated in Fig. 2.

The two phase plates have a thickness of 0.3 mm (closer to the source) and 0.2 mm, respectively. The total effective thickness $t' = t/\cos\theta$ = 0.55 mm. The transmitted beam is 31% of the incident one.

Energy (keV)	χ_1	χ_2	θ_1	θ_2	$P_1' \pm 0.2$	$P_2' \pm 0.2$
7.200 (I)	45	45	+19.5	+19.5	−0.81	−0.04
7.200 (II)	45	135	+19.5	−19.5	−0.89	−0.01
7.200 (III)	45	45	+19.5	−19.5	−0.85	−0.02
7.200 (IV)	45	−45	+19.5	−19.5	−0.96	−0.02

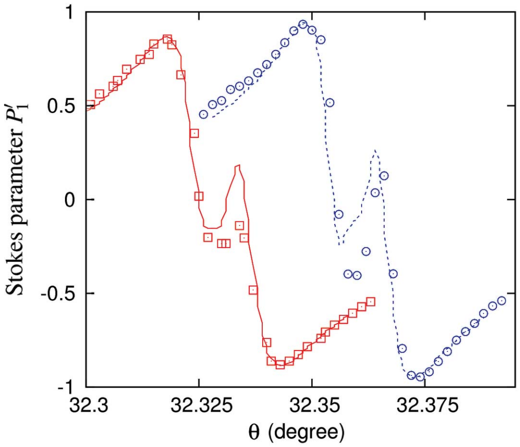

Figure 6
Intensities measured at 5.57 keV with a couple of 0.1 mm phase plates in the unrotated linear polarization channel. Configurations I and IV are represented by (red) squares and (blue) circles, respectively. They are scaled so as to represent P_1'. The two data sets are shifted by 0.03° for clarity. Phase plate 1 delivers a circular polarization and the abscissa is the θ angle of phase plate 2. Lines are fits with a double convolution of the ideal function (see text).

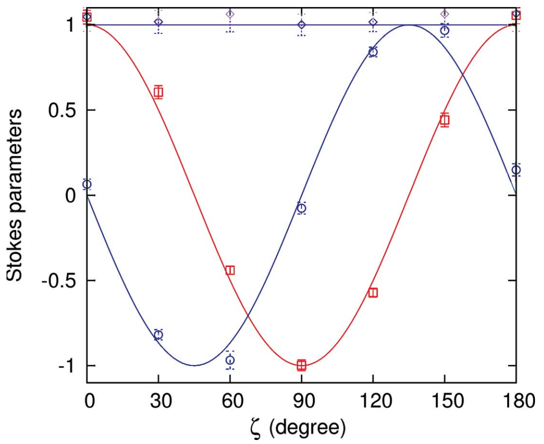

Figure 7
Polarization scan performed on the direct beam at 5.5 keV with a couple of 0.1 mm phase plates. Red squares, blue circles and magenta diamonds represent the measured values of P_1', P_2' and $P_{\rm lin} = [(P_1')^2 + (P_2')^2]^{1/2}$, respectively.

small depolarization arises even from the compensated spread. In configuration (I) the compensated spread is forced to 0, while the uncompensated one, owing to all effects, δE, $\delta\alpha$, $\delta\beta$ (see Table 1), is 0.0025 (2)° root mean square (r.m.s.). In configuration (IV), the uncompensated $\delta\alpha$ is 0.0015 (2)° r.m.s. and the compensated $(\delta E^2 + \delta\beta^2)^{1/2}$ is 0.0020 (4)° r.m.s. Fig. 7 shows the Stokes parameters measured in configuration (IV), with $\Delta\theta_1$, $\Delta\theta_2$ adjusted to the total half-wave shift and rotating χ_1 and χ_2 together ($\zeta = 2\chi_1$, see end of §2). Fig. 8 compares the single-plate configuration with the best result obtained with the two-phase-plate configuration. In the examined energy range the double-diamond set-up provides a 10% improvement compared with a single-diamond system.

In order to underline the importance of this result, which at first glance might not justify the effort of realising a more complicated set-up, it is interesting to calculate the thickness required by a single-phase-plate system to produce a 10% higher polarization rate. It is shown in Appendix *A* that the depolarization produced by a phase plate is inversely proportional to the square of its effective thickness. Using the value for P_1' in Table 2, taken at 3.720 keV, the required thickness $t_{\rm I}^*$ to have the same polarization rate as configuration (IV) with thickness $t_{\rm IV}$ would be

$$t_{\rm I}^* = t_{\rm IV}\left(\frac{P_{1,{\rm I}}'+1}{P_{1,{\rm IV}}'+1}\right)^{1/2} = 2.2\,t_{\rm IV}. \qquad (23)$$

$t_{\rm I}^*$ is obtained considering that given the polarization rate $P_{1,{\rm I}}'$ corresponding to the thickness $t_{\rm I} = t_{\rm IV}$ we are looking for the thickness ($t_{\rm I}^*$) that will produce the wanted polarization rate $P_{1,{\rm IV}}'$. The absorption factor for that $t_{\rm I}^*$ would be roughly 500, about the square of the absorption factor 17 occurring for $t_{\rm IV}$. Therefore, the use of the double phase plates represents a significant advantage.

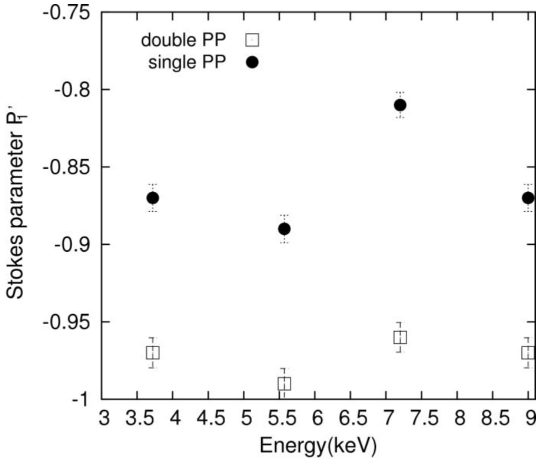

Figure 8
Obtained polarization rate as a function of the incident X-ray energy. Each energy requires a different pair of phase plates.

6. Resonant X-ray diffraction on UO_2

In order to test the double-phase-plate set-up we performed a resonant X-ray diffraction experiment on a sample of UO_2 at the U M_4 edge (3.728 keV). Below the Néel temperature, $T_{\rm N}$ = 31 K, it assumes a complicated magnetic structure of the 3**k** variety (Willis & Taylor, 1965; Frazer *et al.*, 1965; Burlet *et al.*, 1986). Important theories have been developed since the late 1960s (Allen, 1968*a*,*b*; Sasaki & Obata, 1970; Siemann & Cooper, 1979; Solt & Erdös, 1980) up until more recent times (Kudin *et al.*, 2002; Laskowski *et al.*, 2004; Magnani *et al.*, 2005). All these theories emphasize the importance of the interplay between the Jahn–Teller and quadrupolar interactions in UO_2. The evidence for the ordering of the quadrupoles was provided recently by resonant X-ray diffraction at the uranium M_4 edge (Wilkins *et al.*, 2006).

Following Wilkins *et al.* (2006) we write the resonant diffraction amplitude for an electric dipole ($E1$) event as

$$f_{E1}^{\rm res} = f_0 + if_1 + f_2, \qquad (24)$$

where the terms f_n are given by the following equations,

$$f_0 = \hat{\boldsymbol{\varepsilon}}_f\cdot\hat{\boldsymbol{\varepsilon}}_i(F_{11}+F_{1-1}), \qquad (25)$$

$$f_1 = (\hat{\boldsymbol{\varepsilon}}_f\times\hat{\boldsymbol{\varepsilon}}_i)\cdot\hat{\mathbf{z}}(F_{11}-F_{1-1}), \qquad (26)$$

$$f_2 = \hat{\boldsymbol{\varepsilon}}_f\cdot\widetilde{T}\cdot\hat{\boldsymbol{\varepsilon}}_i(2F_{10}-F_{11}-F_{1-1}). \qquad (27)$$

F_{1q} is the resonant energy factor (Hill & McMorrow, 1996), $\hat{\mathbf{z}}$ is the direction of the magnetic moment and $\widetilde{T}$ is a tensor of rank two. $\hat{\boldsymbol{\varepsilon}}_i$ and $\hat{\boldsymbol{\varepsilon}}_f$ represent the direction of the incident and diffracted photon polarization, respectively.

The term f_0 represents Thomson (charge) scattering and equals zero for space-group forbidden reflections. The term f_1 probes a tensor of rank one, with odd time-reversal symmetry arising from a net spin polarization. The term f_2 represents a traceless symmetric tensor of rank two that can arise from an asymmetry intrinsic to the crystal structure (Templeton scattering or anisotropic tensor susceptibility) or it can be due to antiferro order of electric quadrupole moments. It possesses a time-even symmetry. It can be shown (Wilkins *et al.*, 2006) that the reflections arising from quadrupolar ordering coincide with those due to magnetic dipole ordering. The experimental challenge for Wilkins *et al.* (2006) was therefore to separate the two contributions: magnetic dipole and electric quadrupole. They achieved this result by means of diffracted polarization analysis. Indeed, for σ-polarized incident X-rays (the polarization direction is perpendicular to the diffraction plane) all the scattering from the magnetic structure is in the rotated channel σ–π', while the signal from the electric quadrupole might be present in both rotated σ–π' and unrotated σ–σ' channels.

In order to test the double-phase-plate set-up under 'real' conditions we performed first the same experiment as carried out by Wilkins *et al.* (2006) by measuring the azimuthal dependence (scan about the scattering wavevector) of the (112) forbidden reflection in both σ–π' and σ–σ' channels. Then we took advantage of the possibility to change the direction of the incident photon polarization. The goal of these measurements was not to provide better evidence for the quadrupole ordering but to check the sensitivity of the method, given the remarkable difference in the strength of the two signals.

Results from the azimuthal scan follow the expected dependence and are displayed in Fig. 9. The contributions of two transverse domains are taken into account as an incoherent sum of intensities. We show the ratio σ–σ' over σ–π' here as first it gives a straightforward estimate of the magnitude of the two resonant processes. This will play an important role in the analysis of the polarization scans. Secondly, some systematic errors such as the change in the absorption of the sample and a partial illumination of the sample, which might occur as a function of the azimuthal angle, are eliminated by the ratio. These errors are normally significant for off-specular reflections.

The use of phase-plate polarimetry and polarization scans enables the experimenter to eliminate such errors. The measurements are performed with the sample at rest; the sample does not move and only the direction of the incident polarization together with the position of the analyzer crystal is changed. Moreover, polarization scans are very sensitive to the simultaneous presence of two sources of scattering that may (Mazzoli *et al.*, 2007) or may not, as we will see with UO_2, interfere. In this section, unprimed values for P_1 and P_2 refer to the Stokes parameters describing the polarization state of the beam after the phase plates, and primed values refer to the polarization state of the beam after being diffracted by the sample (see Fig. 1).

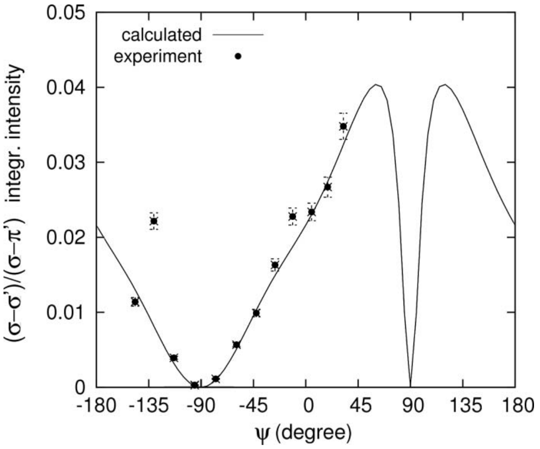

Figure 9
Azimuthal angle dependence for the (112) reflection at the uranium M_4 edge at 12 K. The ratio σ–σ' over σ–π' is shown. Circles represent the experimental data, while the line represents the calculated ratio according to the magnetic and quadrupolar ordering as given by Wilkins *et al.* (2006).

We have selected three different positions in azimuth, $\psi = -95^\circ$, $\psi = -11^\circ$ and $\psi = 32^\circ$. At each position a polarization scan was performed. $\psi = -95^\circ$ was chosen as no quadrupolar signal is expected, $\psi = -11^\circ$ is where the quadrupolar scattering is maximum and $\psi = 32^\circ$ is where the ratio between the quadrupole and the magnetic signal is expected to be maximum (compatible with our experimental geometry limitations). Results are presented in Figs. 10, 11 and 12 for the three azimuthal angles, respectively. For each direction of the polarization (represented by the angle ζ) the analyzer stage is rotated discretely (angle η) and the polarization analyzer is rocked. The set of integrated intensities obtained by the latter scans are subsequently fitted using (22). The fit enables the extraction of the P_1' and P_2' Stokes parameters. The experimental values of the Stokes parameters are then compared with their expected values. The latter can be readily calculated once the magnetic and quadrupolar structure factors are known. An instructive example on how to perform such a calculation can be found by Fernández-Rodríguez *et al.* (2008). For $\psi = -95^\circ$, no quadrupole contribution is expected and therefore all the observed intensity comes from magnetic scattering. Comparing predictions with experimental results is straightforward. Indeed the agreement is rather good as can be seen in Fig. 10.

Now we turn our attention to the other two polarization scans which are illustrated in Figs. 11 and 12. At first we tried to fit the data only with the magnetic contribution (continuous line). The agreement with experimental results is already remarkable. Only minor differences are visible. However, these tiny differences are exactly the signature of the presence of the quadrupolar ordering. Including the quadrupolar contribution to the calculated scattering amplitude leads to an improvement in the description of the experimental data. The model calculation including both contributions (without interference) is represented in the figures by a dashed line. One possible explanation for the lack of interference is that this term may be cancelled between two domains. The calculations are performed by utilizing a single parameter, which represents the ratio between the quadrupole and magnetic contribution in the scattering amplitude. In our case this parameter has been determined by the azimuthal angle scan illustrated in Fig. 9. The small difference between the two models reflects the weakness of the quadrupole scattering compared with the magnetic one. From Fig. 9 one can readily estimate that the contribution of quadrupole scattering barely exceeds 4% of the magnetic signal. Nevertheless, such a small signal gives a sizeable contribution in the polarization scans.

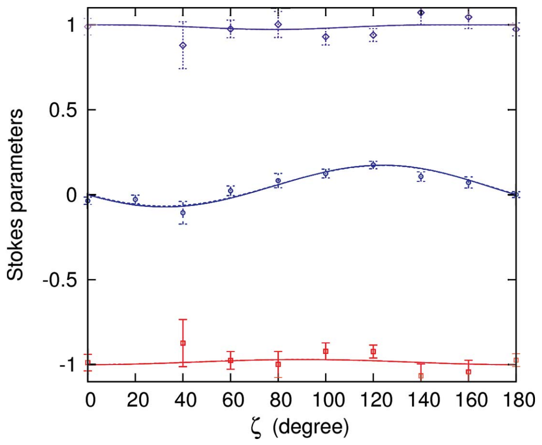

Figure 10
Polarization scan for the (112) reflection at the uranium M_4 edge at 12 K, $\psi = -95°$. Red squares, blue circles and magenta diamonds represent the measured values of P_1', P_2' and $P_{\rm lin} = [(P_1')^2 + (P_2')^2]^{1/2}$, respectively. The lines, following the same colour code, represent the calculated Stokes parameters according to the magnetic (continuous lines) and magnetic plus quadrupolar (dashed lines) ordering as proposed by Wilkins *et al.* (2006).

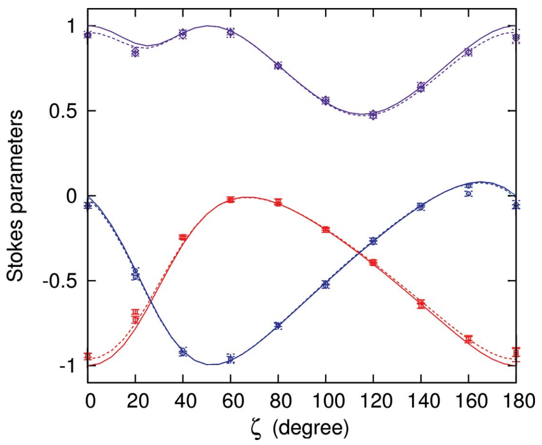

Figure 11
Polarization scan for the (112) reflection at the uranium M_4 edge at 12 K, $\psi = -11°$. Red squares, blue circles and magenta diamonds represent the measured values of P_1', P_2' and $P_{\rm lin} = [(P_1')^2 + (P_2')^2]^{1/2}$, respectively. The lines, following the same colour code, represent the calculated Stokes parameters according to the magnetic (continuous lines) ordering and magnetic plus quadrupolar (dashed lines) ordering as proposed by Wilkins *et al.* (2006).

To conclude, with the use of polarization scans we have disentangled the magnetic and quadrupole contributions of the diffracted intensity. This result proves important as it shows the sensitivity of this technique, even in the case where one signal is only a few percent of the other.

7. Conclusions

The use of a double-phase-plate set-up produces a 10% higher rotated polarization rate compared with a system with a single phase plate of equal total thickness over the energy range examined (3.7–7.2 keV). These results are particularly interesting for resonant X-ray scattering applications, especially at the uranium M edges, where, to obtain the same rate of rotated polarization, the transmitted beam is attenuated 50 times less thanks to the presence of the two retarders.

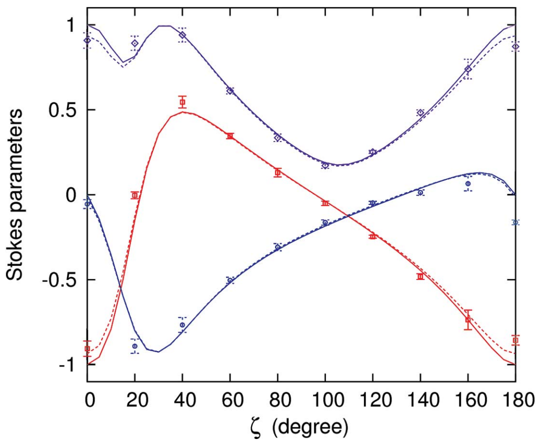

Figure 12
Polarization scan for the (112) reflection at the uranium M_4 edge at 12 K, $\psi = 32°$. Red squares, blue circles and magenta diamonds represent the measured values of P_1', P_2' and $P_{\rm lin} = [(P_1')^2 + (P_2')^2]^{1/2}$, respectively. The lines, following the same colour code, represent the calculated Stokes parameters according to the magnetic (continuous lines) and magnetic plus quadrupolar (dashed lines) ordering as proposed by Wilkins *et al.* (2006).

In order to test the set-up in the most interesting energy range, we have performed a resonant X-ray scattering experiment on UO_2 at the uranium M_4 edge. By taking advantage of the possibility to rotate the direction of the incoming photon polarization we show that it is possible to disentangle the quadrupole and magnetic diffraction contributions. Therefore, polarization scans might be regarded as a complementary and/or alternative means to investigate samples by use of X-ray diffraction. Whilst this approach shows all its benefits when interference occurs between two scattering events, this is not the case for UO_2.

APPENDIX *A*
Phase plate thickness and depolarization effects

If we recall the expression for P_1' given in (13), with $\varphi = \Delta\varphi$ to ease notation, we have

$$P_1' = 1 + [\cos(\varphi) - 1]\sin(2\chi)^2, \qquad (28)$$

to have linear light rotated by 90°, where χ will be $\pm\pi/4$ and $\varphi^* = -\pi$. If we expand P_1' in the vicinity of φ^* we have

$$P_1'(\delta\varphi) \simeq -1 + (1/2)(\delta\varphi)^2, \qquad (29)$$

where $\delta\varphi$ represents a distribution about the actual setting φ^*. Then,

$$\langle P_1' \rangle \simeq -1 + (1/2)\langle \delta\varphi^2 \rangle. \qquad (30)$$

Now if we rewrite (9) as $\varphi = kt/\Delta\theta$ with k constant and we differentiate on both sides, we obtain

$$\delta\varphi = -\frac{kt}{(\Delta\theta)^2}\,\delta(\Delta\theta) = -\frac{\varphi^2}{kt}\,\delta(\Delta\theta). \qquad (31)$$

Looking back at (30) we obtain

$$\langle P_1'\rangle = -1 + \frac{\varphi^4}{2k^2t^2}\langle\delta(\Delta\theta)\rangle^2, \tag{32}$$

which shows that the degradation in the produced rotated light is inversely proportional to the square of the effective thickness of the retarder.

APPENDIX *B*
Convolution of angular spreads

The aim is to calculate the Stokes parameter P_1' for a beam made of angularly spread rays, after going through two phase plates. Two approximations are made: first, the anomalous absorption close to the Bragg angle is neglected; second, the correlation between the energy deviation δE and the vertical deviation $\delta\beta$ is ignored, though such a correlation is produced by the monochromator. Equation (9) is rewritten for two plates as

$$\Delta\varphi = \frac{K_1}{\Delta\theta_1} + \frac{K_2}{\Delta\theta_2}. \tag{33}$$

K_1 is different from K_2 if the plate thicknesses are different. Through (13) and (33) P_1' is a function of $(\Delta\theta_1, \Delta\theta_2)$ and, since the total intensity is invariant for small $\Delta\theta$, the value of P_1' is obtained by summation of its values for individual rays. We represent the beam as a Gaussian distribution in $(\Delta\theta_1 + \Delta\theta_2)$ and $(\Delta\theta_1 - \Delta\theta_2)$,

$$\frac{1}{\pi s d}\exp\left[-\frac{(\Delta\theta_1+\Delta\theta_2)^2}{2s^2} + \frac{(\Delta\theta_1-\Delta\theta_2)^2}{2d^2}\right], \tag{34}$$

where s and d are r.m.s. spreads in the two directions. The sum of $\Delta\theta$ is not compensated whereas the difference is. They represent deviations along horizontal $\delta\alpha$, vertical $\delta\beta$ and energy δE, combined as indicated in Table 1; energy is converted to angles through Bragg's law. The integration of P_1' over the resolution function (34) is performed numerically.

We wish to thank R. Caciuffo for fruitful discussions and for providing the UO_2 sample. We also thank J. Hartwig who provided the phase plates and carried out their topographic characterization.

References

Allen, S. J. (1968*a*). *Phys. Rev.* **166**, 530–539.

Allen, S. J. (1968*b*). *Phys. Rev.* **167**, 492–496.

Blume, M. & Gibbs, D. (1988). *Phys. Rev. B*, **37**, 1779–1789.

Born, M. & Wolf, E. (1999). *Principle of Optics*, 7th ed. Cambridge University Press.

Burlet, P., Rossat-Mignod, J., Quezel, S., Vogt, O., Spirlet, J. C. & Rebizant, J. (1986). *J. Less Common Metals*, **121**, 121–139.

Fabrizi, F., Walker, H. C., Paolasini, L., de Bergevin, F., Boothroyd, A. T., Prabhakaran, D. & McMorrow, D. F. (2009). *Phys. Rev. Lett.* **102**, 237205.

Fano, U. (1957). *Rev. Mod. Phys.* **29**, 74–93.

Fernández-Rodríguez, J., Lovesey, S. W. & Blanco, J. A. (2008). *Phys. Rev. B*, **77**, 094441.

Frazer, B. C., Shirane, G., Cox, D. E. & Olsen, C. E. (1965). *Phys. Rev.* **140**, A1448–A1452.

Gibbs, D. G., Harshman, D. R., Isaacs, E. D., McWhan, D. B., Mills, D. & Vettier, C. (1988). *Phys. Rev. Lett.* **61**, 1241–1244.

Giles, C., Malgrange, C., de Bergevin, F., Vettier, C., Yakhou, F. & Stunault, A. (1997). Unpublished.

Giles, C., Malgrange, C., Goulon, J., de Bergevin, F., Goulon, J., Baudelet, F., Fontaine, A., Vettier, C. & Freund, A. (1995). *Nucl. Instrum. Methods Phys. Res. A*, **361**, 354–357.

Giles, C., Malgrange, C., Goulon, J., de Bergevin, F., Vettier, C., Dartyge, E., Fontaine, A., Giorgetti, C. & Pizzini, S. (1994). *J. Appl. Cryst.* **27**, 232–240.

Golovchenko, J. A., Kincaid, B. M., Levesque, R. A., Meixner, A. E. & Kaplan, D. R. (1986). *Phys. Rev. Lett.* **57**, 202–205.

Hill, J. P. & McMorrow, D. F. (1996). *Acta Cryst.* A**52**, 236–244.

Hirano, K., Izumi, K., Ishikawa, T. & Annaka, S. (1991). *Jpn. J. Appl. Phys.* **30**, L407–L410.

Isaacs, E. D., McWhan, D. B., Peters, C., Ice, G. E., Siddons, D. P., Hastings, J. B., Vettier, C. & Vogt, O. (1989). *Phys. Rev. Lett.* **62**, 1671–1674.

Johnson, R. D., Bland, S. R., Mazzoli, C., Beale, T. A. W., Du, C.-H., Detlefs, C., Wilkins, S. B. & Hatton, P. D. (2008). *Phys. Rev. B*, **78**, 104407.

Kudin, K. N., Scuseria, G. E. & Martin, R. L. (2002). *Phys. Rev. Lett.* **89**, 266402.

Laskowski, R., Madsen, G. K. H., Blaha, P. & Schwarz, K. (2004). *Phys. Rev. B*, **69**, 140408.

Magnani, N., Santini, P., Amoretti, G. & Caciuffo, R. (2005). *Phys. Rev. B*, **71**, 054405.

Mazzoli, C., Wilkins, S. B., Matteo, S. D., Detlefs, B., Detlefs, C., Scagnoli, V., Paolasini, L. & Ghigna, P. (2007). *Phys. Rev. B*, **76**, 195118.

Murakami, Y., Hill, J. P., Gibbs, D., Blume, M., Koyama, I., Tanaka, M., Kawata, H., Arima, T., Tokura, Y., Hirota, K. & Endoh, Y. (1998). *Phys. Rev. Lett.* **81**, 582–585.

Okitsu, K., Ueji, Y., Sato, K. & Amemiya, Y. (2001). *J. Synchrotron Rad.* **8**, 33–37.

Paolasini, L., Detlefs, C., Mazzoli, C., Wilkins, S., Deen, P. P., Bombardi, A., Kernavanois, N., de Bergevin, F., Yakhou, F., Valade, J. P., Breslavetz, I., Fondacaro, A., Pepellin, G. & Bernard, P. (2007). *J. Synchrotron Rad.* **14**, 301–312.

Paolasini, L., Vettier, C., de Bergevin, F., Yakhou, F., Mannix, D., Stunault, A., Neubeck, W., Altarelli, M., Fabrizio, M., Metcalf, P. A. & Honig, J. M. (1999). *Phys. Rev. Lett.* **82**, 4719–4722.

Sasaki, K. & Obata, Y. (1970). *J. Phys. Soc. Jpn*, **28**, 1157–1167.

Scagnoli, V., Staub, U., Mulders, A. M., Janousch, M., Meijer, G. I., Hammerl, G., Tonnerre, J. M. & Stojic, N. (2006). *Phys. Rev. B*, **73**, 100409(R).

Siemann, R. & Cooper, B. R. (1979). *Phys. Rev. B*, **20**, 2869–2885.

Solt, G. & Erdös, P. (1980). *Phys. Rev. B*, **22**, 4718–4726.

Templeton, D. H. & Templeton, L. K. (1982). *Acta Cryst.* A**38**, 62–67.

Wilkins, S. B., Caciuffo, R., Detlefs, C., Rebizant, J., Colineau, E., Wastin, F. & Lander, G. H. (2006). *Phys. Rev. B*, **73**, 060406.

Willis, B. & Taylor, R. (1965). *Phys. Lett.* **17**, 188–190.